ACS Chemical Neuroscience

Research Article

pubs.acs.org/chemneuro

Spontaneous Inward Opening of the Dopamine Transporter Is Triggered by PIP_2-Regulated Dynamics of the N-Terminus

George Khelashvili,*[,†] Nathaniel Stanley,[‡] Michelle A. Sahai,[†] Jaime Medina,[†] Michael V. LeVine,[†] Lei Shi,[†,§] Gianni De Fabritiis,[‡,∥] and Harel Weinstein[†,§]

[†]Department of Physiology and Biophysics, Weill Cornell Medical College of Cornell University (WCMC), New York, New York 10065, United States

[‡]Computational Biophysics Laboratory (GRIB-IMIM), Universitat Pompeu Fabra, Barcelona Biomedical Research Park (PRBB), C/Doctor Aiguader 88, 08003 Barcelona, Spain

[§]HRH Prince Alwaleed Bin Talal Bin Abdulaziz Alsaud Institute of Computational Biomedicine, Weill Cornell Medical College of Cornell University, New York, New York 10065, United States

[∥]Institució Catalana de Recerca i Estudis Avançats, Passeig Lluis Companys 23, 08010 Barcelona, Spain

Supporting Information

ABSTRACT: We present the dynamic mechanism of concerted motions in a full-length molecular model of the human dopamine transporter (hDAT), a member of the neurotransmitter/sodium symporter (NSS) family, involved in state-to-state transitions underlying function. The findings result from an analysis of unbiased atomistic molecular dynamics simulation trajectories (totaling >14 μs) of the hDAT molecule immersed in lipid membrane environments with or without phosphatidylinositol 4,5-biphosphate (PIP_2) lipids. The N-terminal region of hDAT (N-term) is shown to have an essential mechanistic role in correlated rearrangements of specific structural motifs relevant to state-to-state transitions in the hDAT. The mechanism involves PIP_2-mediated electrostatic interactions between the N-term and the intracellular loops of the transporter molecule. Quantitative analyses of collective motions in the trajectories reveal that these interactions correlate with the inward-opening dynamics of hDAT and are allosterically coupled to the known functional sites of the transporter. The observed large-scale motions are enabled by specific reconfiguration of the network of ionic interactions at the intracellular end of the protein. The isomerization to the inward-facing state in hDAT is accompanied by concomitant movements in the extracellular vestibule and results in the release of an Na^+ ion from the Na2 site and destabilization of the substrate dopamine in the primary substrate binding S1 site. The dynamic mechanism emerging from the findings highlights the involvement of the PIP_2-regulated interactions between the N-term and the intracellular loop 4 in the functionally relevant conformational transitions that are also similar to those found to underlie state-to-state transitions in the leucine transporter (LeuT), a prototypical bacterial homologue of the NSS.

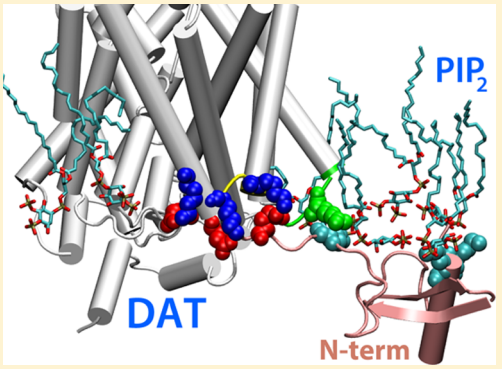

KEYWORDS: *Neurotransmitter transporter, NSS, LeuT, alternating access, molecular dynamics simulation, electrostatics, allosteric coupling*

Members of the neurotransmitter/sodium symporter (NSS) family, which include the human transporters for dopamine (DAT), serotonin (SERT), and norepinephrine (NET), are transmembrane (TM) proteins whose main physiological function is considered to be the termination of a neuronal signal by reuptake of the neurotransmitter from the synaptic cleft into the presynaptic neuronal cell.[1−7] The uptake of neurotransmitter against its concentration gradient is coupled to the transport of Na^+ into the cell.[3] The reuptake function of the NSS in neuronal signaling accords them vital roles in cognitive, emotional, and behavioral functions and in various psychiatric and neurological disorders[8] making them primary targets for antidepressants as well as for abused psychostimulants.[9,10] More recently, specific *de novo* mutations in human DAT (hDAT) have been associated with various neurological diseases.[11−19]

The available X-ray models of DAT from *Drosophila* (dDAT)[20,21] show a remarkable similarity between the TM bundles of dDAT and the bacterial leucine transporter (LeuT), for which several crystal structures corresponding to various functional states (i.e., outward open, occluded, and inward open) had been determined earlier.[22−29] Their sequence homology had suggested the same 12-TM helical bundle architecture (including 10-TM core region),[30] a centrally located primary substrate

Received: July 2, 2015
Published: August 8, 2015

DOI: 10.1021/acschemneuro.5b00179
ACS Chem. Neurosci. 2015, 6, 1825−1837

binding site (the S1 site), and two Na^+ binding sites, Na1 and Na2.[31−37]

The availability of structural information had prompted the formulation of a unified mechanistic model of the transport cycle in NSS proteins that is consistent with the alternating access mechanism.[38] Structure/function studies of bacterial LeuT-fold transporters conducted *in vitro* with double electron−electron resonance (DEER) and single molecule FRET (smFRET),[39−43] measurements of ligand binding and transport in LeuT,[44,45] as well as computational simulations of LeuT[39−42,44,46−54] and of homology models of DAT[33−37] and SERT,[55,56] have provided important mechanistic insights into ion- and ligand-dependent conformational dynamics in NSS, suggesting that the alternating access is achieved through concerted dynamic rearrangements involving specific structural motifs of these proteins. The results of such studies have further led to a proposed mechanistic model of allosteric Na^+-coupled symport in which intracellular release of the S1-bound substrate is triggered by the binding of a second substrate molecule in the extracellular vestibule located ∼11 Å above the S1 site, termed the S2 site.[44]

The focused attention on LeuT has produced a large amount of structural and functional information that underscores the importance of establishing to what extent the knowledge accumulated from this bacterial homologue can explain the corresponding functional mechanisms in the mammalian NSS transporters, at the same detailed molecular level. In spite of the great structural similarity revealed for the TM domains of LeuT and the eukaryotic NSS, it is clear that the long N- and C-terminal regions found only in the eukaryotic transporters but not in LeuT, represent a major difference that is likely to be of significant functional importance. These segments have been implicated in key mechanistic elements of NSS function including regulatory phosphorylation[57−62] and the actions of psychostimulants.[57,58,63−66] Indeed, the involvement of the N-terminal domain (N-term) in amphetamine (AMPH)-induced reverse transport (efflux) of the substrate has been well documented for the neurotransmitter transporters.[57,63,64,67−70] In hDAT, specifically, the AMPH-induced efflux has been shown to be modulated by the first (distal from the TM bundle) 22 residues in the hDAT N-term.[66] Their electrostatic interactions with highly charged phosphatidylinositol 4,5-biphosphate (PIP_2) lipids[71] and phosophorylation of this region at one or multiple Ser residues (see Figure S1A−B)[57] were implicated in the mechanism of the AMPH-induced efflux.

Reasoning that an understanding of the mechanisms underlying the functional role of the terminal domains can reveal important aspects of state-to-state transitions in the NSS transporters necessary for the phenotypes that were shown to involve the N-term, we have undertaken, to our knowledge for the first time, an analysis of the possible role of the N-term in these molecular mechanisms in a full-length model of the hDAT. The analysis of the dynamics and functionally relevant conformational transitions of the transporter was carried out on extensive (>14 μs in total time) unbiased atomistic molecular dynamics (MD) trajectories of the hDAT in physiologically relevant lipid membrane environments (enriched in PIP_2 lipids). The results outline initial steps of the spontaneous transition of the transporter from a starting outward-facing state to an inward-facing state, examined from rearrangements in specific structural motifs previously identified in LeuT, and culminating in the release of Na^+ from the Na2 site and in destabilization of the substrate in the S1 site. We determined the manner in which these steps are regulated by the membrane environment and found that the state-to-state transitions in hDAT can be triggered by PIP_2-mediated electrostatic association between the N-terminal domain and the intracellular loop 4 (ICL4). Specifically, we show here that the N-term/ICL4 complex is stabilized by PIP_2 and can be formed through involvement of either the distal region of the N-term (i.e., the most N-terminal end, containing residues K3 and K5) or by the region proximal to the TM bundle (containing R51). Together, the results of this computational study provide novel insights into the role of collective dynamics in functionally relevant state-to-state transitions in the transporter, at a level of atomistic detail that enables specific experimental probing of the mechanistic hypotheses regarding essential functional mechanisms of the NSS transporters.

RESULTS AND DISCUSSION

We have recently demonstrated both experimentally and computationally that the first 64-residue long N-terminal fragment of the hDAT associates with lipid membranes through electrostatic interactions with PIP_2 lipids.[71,72] To provide a structural context for these interactions in the full-length hDAT protein and to evaluate the role of PIP_2-mediated intramolecular associations in functionally relevant conformational transitions in the transporter, we constructed full-length hDAT models (see Methods) and studied their conformational dynamics with extensive unbiased atomistic MD simulations (see Figure 1) in an explicit PIP_2-containing lipid membrane and solvent environment. The findings from these computational studies are presented in depth below and are compared to the results obtained from the analysis of the control trajectories of hDAT collected in PIP_2-depleted bilayers as described in Figure 1.

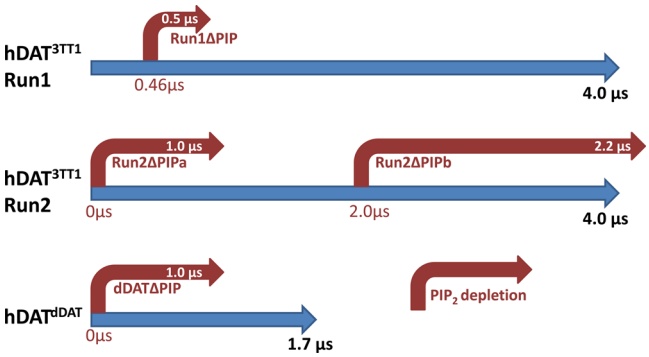

Figure 1. Schematic representation of the atomistic MD simulations performed on $hDAT^{3TT1}$ and $hDAT^{dDAT}$ constructs embedded in lipid membranes. Two original trajectories (Run1 and Run2) for the $hDAT^{3TT1}$ model in Na^+Cl^- solution and a single run of $hDAT^{dDAT}$ in K^+Cl^- solution were accumulated in PIP_2-enriched lipid membranes (simulation times are indicated in bold at the ends of the thick blue arrows). At various time-points in these trajectories (indicated with red arrows), PIP_2 lipids were substituted with POPE lipids, and the control simulations (identified as ΔPIP) were restarted. The subsequent MD trajectories are correspondingly labeled (Run1ΔPIP, Run2ΔPIPa, Run2ΔPIPb, and dDATΔPIP), and their durations are shown on top of the respective red arrows.

N-Terminus of hDAT Associates with the ICL4 Loop through PIP_2-Mediated Interactions. Monitoring the dynamics of the N-terminal domain during a 1.7 μs trajectory of the $hDAT^{dDAT}$ model showed that the N-term, which was initially placed away from the TM bundle and the lipid membrane (Figure S3B), engages with PIP_2 lipids and associates with the ICL4 segment (residues H442-R443-H444) over the

DOI: 10.1021/acschemneuro.5b00179
ACS Chem. Neurosci. 2015, 6, 1825−1837

course of the simulation. Specifically, the basic residues in the N-term gradually establish interactions with PIP_2 lipids within the first 0.2 μs of the $hDAT^{dDAT}$ trajectory, as detailed in Figure S4A. During the same time interval, the N-term moves closer to the ICL4 loop, as the K3 residue of the N-term approaches R443 (see Figure S4B). Later in the trajectory, other basic residues in the N-term, most notably R51 (but also K35, albeit more transiently), engage with the ICL4 loop as well (Figure S4B).

Since the ICL4 is itself highly polar as it contains, in addition to R443, two neighboring His residues, we reasoned that PIP_2 lipids would be involved as well in the association between the N-term and the ICL4 through electrostatic forces. Indeed, quantification of the proximity of PIP_2 lipid molecules to different regions of the transporter, identified ICL4 as one of the areas that was most densely populated with surrounding PIP_2 lipids (Figure S5); indeed, R443 is among the specific residues contacting PIP_2 most frequently (Figure 2C). Of note, the ICL4 region containing

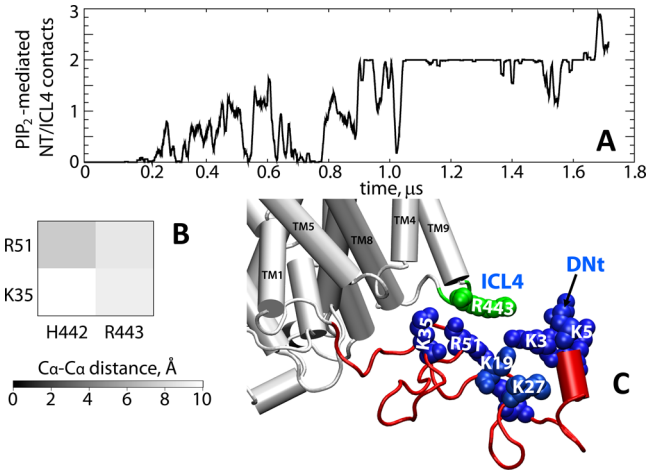

Figure 2. HDAT N-term interacts with ICL4 and PIP_2 lipids in a 1.7 μs long $hDAT^{dDAT}$ trajectory (also Figure S4). (A) Number of PIP_2 lipids in contact with the interacting polar residues from the N-term (K3, K5, K27, K35, and R51) and ICL4 (H442, R443, and H444) presented as the moving average over 1 ns windows. Contact is defined by Cα-Cα distance of the interacting pair (within 9 Å), and any atom of PIP_2 within 3 Å of both residues. (B) Cα-Cα distances for N-term/ICL4 residue pairs averaged over the second half of the $hDAT^{dDAT}$ trajectory. Only the pairs within 9 Å are shown. (C) Residues within 3 Å of a PIP_2 lipid headgroup in >80% of the trajectory are shown in space fill format (blue for N-term; green for ICL4). The N-term is rendered in red, and the neighboring region is shown in white cartoon format. A black arrow indicates the position of the distal segment of the N-terminus (DNt).

R443 overlaps with residue K460 in SERT, which has been suggested to be critical for PIP_2 binding[73] (R443 and H444 in hDAT align in sequence with SERT A459 and R461, respectively).

Analysis of the time evolution of the N-term/ICL4 association and of the contacts between the interacting residues in these segments and the nearest PIP_2 lipids (Figure 2A) showed that PIP_2-mediated interactions between the N-term and ICL4 first occur at ~0.2 μs into the $hDAT^{dDAT}$ trajectory and rise gradually to a value of about two contacts per time frame. A similarly strong tendency for the formation of the N-term/ICL4 complex involving PIP_2 was observed in the simulations carried out with the $hDAT^{3TT1}$ model (Figure S6A). Interestingly, however, in the $hDAT^{3TT1}$ trajectories the N-term was observed to engage with the ICL4 segment through both its proximal (harboring R51) and its distal ends (including K3/K5) (see Figures S6B and S6D).

In the control MD simulations initiated from intermediate time-points along $hDAT^{3TT1}$Rn1 and $hDAT^{3TT1}$Run2 (0.46 and 2.0 μs, respectively; see Figure 1), in which PIP_2 lipids were replaced by POPE, the N-term/ICL4 complex that was stabilized by PIP_2 dissociated rapidly (C_α-C_α distances between any pair of N-term/ICL4 residues became >10 Å). Importantly, in the additional MD trajectories in which PIP_2 lipids were substituted with POPE in the initial configurations of the $hDAT^{3TT1}$Run2 and $hDAT^{dDAT}$ systems (Run2ΔPIPa and dDATΔPIP trajectories in Figure 1), the N-terminus remained mostly in the solvent, away from ICL4 (data not shown). Collectively, these results suggest that the association of the N-terminus with the ICL4 segment is stabilized by the electrostatic contribution of PIP_2 lipids and can involve both the distal end of the N-terminal segment (K3/K5 residues) and its proximal region (R51 residue). Note that the involvement of the K3/K5 pair in interactions with PIP_2 lipids in all our simulations is consistent with the experimental findings we described[71] regarding the effect of charge-neutralizing mutations in these residues (either to Ala or to Asn) which resulted in reduced binding of the N-term to PIP_2-containing liposomes (see Discussion).

PIP_2-Mediated N-term/ICL4 Association Destabilizes the Functionally Important IC Network of Ionic Interactions. We next reasoned that the N-term/ICL4 association described above could influence the functionally important network of the conserved residues[36,74] in the intracellular end of the transporter, near the N-term and ICL4 segments. The available X-ray structures of LeuT and dDAT, as well as functional assays conducted on hDAT,[36] suggest that the inward-closed state in hDAT is stabilized by salt bridges formed between R60 (in the N-term) and D436 (in TM8 that connects to ICL4), as well as between Y335 (in ICL3) and E428 (in TM8). Interestingly, the dDAT X-ray structure[20] suggests that the IC network in the inward closed DAT contains an additional salt bridge, not present in LeuT, formed between E428 and the conserved R445 residue adjacent to the ICL4.

In our simulations, the IC network of salt bridges becomes destabilized at the onset of the PIP_2-mediated N-term/ICL4 interactions (Figure 3). We observe the disruption of the R60-D436, E428-Y335, and E428-R445 contacts at ~0.2 μs time point of the $hDAT^{dDAT}$ trajectory (Figure 3A–C), when the N-term/ICL4 complex is first formed (Figure 2A). As the extent of the N-term/ICL4 association strengthens (between 0.2 and 0.6 μs), a new salt bridge, formed between residues D436 and R445, is stabilized (Figure 3D–G).

Similar tendencies are observed in the $hDAT^{3TT1}$Run1 and $hDAT^{3TT1}$Run2 simulations. Thus, the R60-D436 and Y335-R445 interactions break in these trajectories as well (Figure S6C) when the N-term engages with the ICL4 (Figure S6A). Concomitantly, the D436-R445 ionic interaction is stabilized (D436-R445 minimum distance is <2.5 Å in these simulations). Importantly, in the two independent control MD trajectories of hDAT carried out in the PIP_2-depleted membranes (dDATΔPIP and Run2ΔPIPb), in which the N-term did not engage with the ICL4 (see above), the Y335-E428 salt bridge, suggested to be the most influential for the stability of the inward closed state,[74] was essentially retained, and the IC gates remained largely closed (Figure S7A–B). Collectively, the above data suggests that PIP_2-mediated N-term/ICL4 association leads to the destabilization of the IC network of ionic interactions. Since the latter has been suggested to be of critical importance for the stability of the

DOI: 10.1021/acschemneuro.5b00179
ACS Chem. Neurosci. 2015, 6, 1825–1837

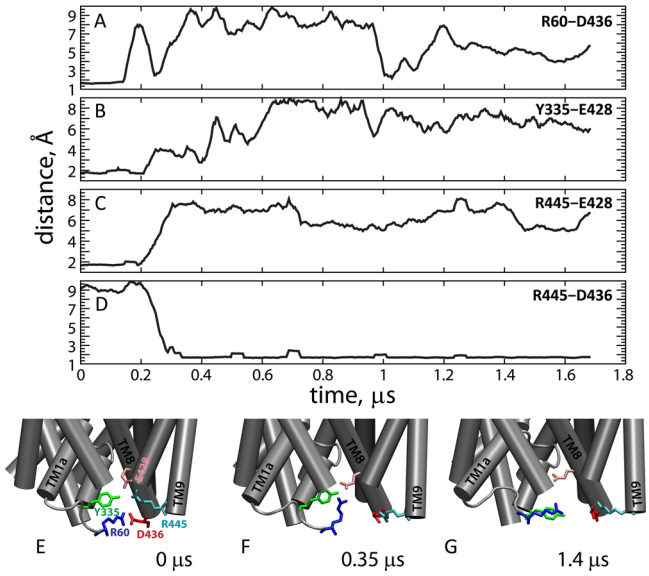

Figure 3. (A–D) Time evolution in the hDAT^{dDAT} simulation of the minimal distance between residue pairs: (A) R60 and D436; (B) Y335-E428; (C) R445-E428; and (D) R445-D436. Panels (E–G) show snapshots of the system at 0 μs (E), 0.35 μs (F), and 1.4 μs (G) time-points along the trajectory, highlighting changes in the positioning of R60 (blue), D436 (red), Y335 (green), E428 (pink), and R445 (cyan) during the simulation. The relevant IC segments of the protein are shown in cartoon rendering. TM1a, TM8, and TM9 are labeled.

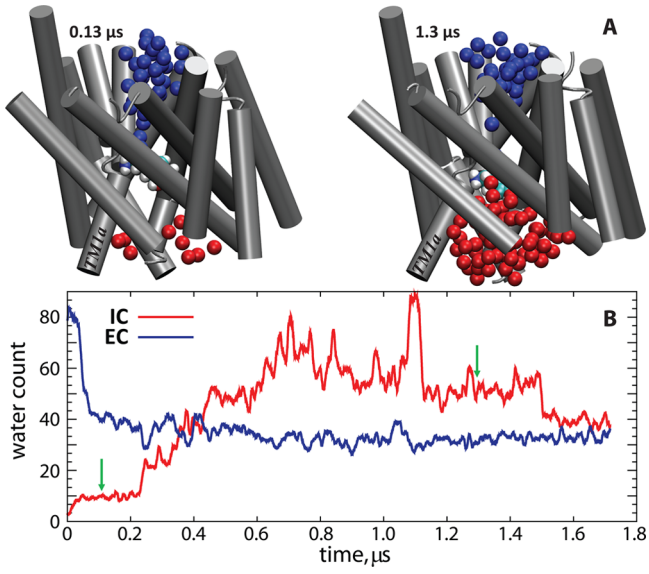

Figure 4. (A) Snapshots of the hDAT TM bundle (gray cartoon) in the hDAT^{dDAT} trajectory at 0.13 and 1.3 μs time-points. Red and blue spheres represent oxygen atoms of the water molecules in the IC and EC vestibules, respectively (see Methods for description of the water count algorithm). The substrate, DA, is shown in van der Waals rendering. The TM1a segment is labeled. (B) Time evolution of the number of water molecules in the IC (red) and EC (blue) vestibules in the hDAT^{dDAT} simulation. The green arrows denote time-points at which the snapshots in panel A were taken.

inward closed state of the transporter,[36] we next examined the conformational dynamics of the hDAT in response to the PIP_2-mediated N-term/ICL4 interactions.

hDAT Undergoes Spontaneous Outward-Facing to Inward-Facing Isomerization in PIP_2-Enriched Membranes. Recent experimental studies of conformational dynamics in LeuT[39−42] and the structurally related Mhp1[43] transporter using single molecule and ensemble spectroscopy measurements, respectively, uncovered structural rearrangements that mark the functionally relevant transitions in the LeuT-like fold NSS proteins. The distance changes between specific loci in IC and EC segments in response to ion and/or ligand binding are attributable to isomerization of these transporters between different functional states (i.e., outward-facing, inward-facing, and occluded). In describing conformational transitions in our simulations, we monitored the same sets of distances between the analogous IC and EC sites in the hDAT and quantified the accumulation of water molecules at the IC and EC vestibules of the transporter during the MD trajectories.

Markers for Opening of the Intracellular Vestibule in hDAT Are Similar to Those in LeuT. Figure 4 shows the count of water molecules inside the EC and IC vestibules during hDAT^{dDAT} simulation, which indicates a rapid (within the first 50 ns of the simulations) loss of hydration in the EC vestibule and increase in water count in the IC vestibule with the transitioning of the transporter from the initially outward-facing state to the occluded state (Figure 4B). This isomerization is due to a relaxation of the protein structure to occlude the substrate DA in the S1 site from the EC vestibule. After this initial equilibration, the transporter remains in the occluded state for the next ~150 ns of the trajectory, which is followed by large-scale concerted motions of the intracellular TM1a, TM6b, and TM9 segments. Indeed, distance measurements between various IC regions of the transporter (Figure 5A–C) reveal that during the subsequent

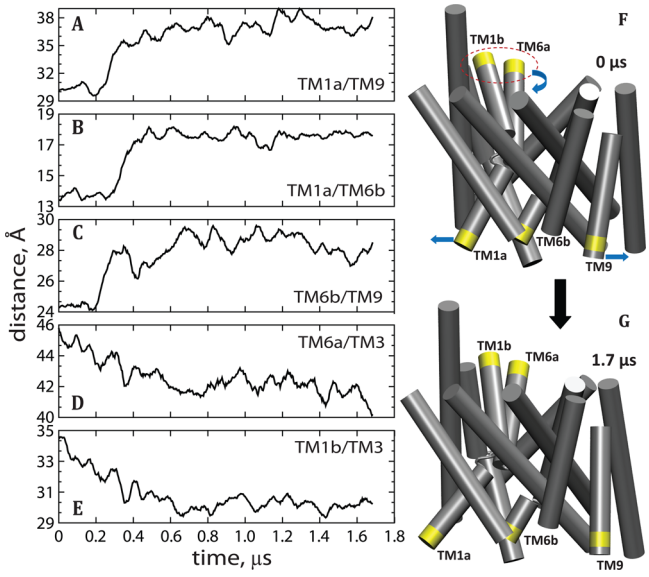

Figure 5. Time evolution in the hDAT^{dDAT} simulation of C_β-C_β distances between residues in various TM segments: (A) I67 (in TM1a) and L447 (in TM9); (B) I67 (in TM1a) and S333 (in TM6b); (C) S333 (in TM6b) and L447 (in TM9); (D) E307 (in TM6a) and F171 (in TM3); and (E) F171 (in TM3) and K92 (in TM1b). Panels F and G depict conformations of the hDAT TM bundle (silver) in the initial and final frames of the trajectory. The IC and EC segments from panels A–E are labeled and colored in yellow. Blue arrows in panel F indicate the direction of movement of the different regions in the transition from F to G. Collective motions of TM1b and TM6a segments are highlighted by a red dotted oval.

~0.2–0.6 μs trajectory interval TM1a-TM6b, TM1a-TM9, and TM6b-TM9 distances increase by ~4.5 Å, 8 Å, and 5 Å,

DOI: 10.1021/acschemneuro.5b00179
ACS Chem. Neurosci. 2015, 6, 1825−1837

respectively. As a result, the TM1a and TM9 segments swing away from the TM bundle (Figure 5F−G) and the IC vestibule opens, allowing the large influx of water molecules (see red trace in Figure 4B).

As seen in Figure S8, during the time period of the trajectory when the IC vestibule widens (0.2−0.6 μs) several other IC segments undergo large-scale motions. Most notably, we observe the displacement of TM7a with respect to ICL1 and TM4, as well as an increase in TM1a-ICL4 and TM2-TM5 distances. Collectively, the data in Figures 5A−C and S8 indicate that the hDAT^{dDAT} simulation captures an inward-opening event in hDAT that follows dynamic trends, which are consonant with DEER distance measurements[39] in LeuT. These DEER measurements showed that TM1a, NT (the fragment of the N-terminus adjacent to TM1a), TM6b, and TM7a undergo the most substantial ion- or ligand-dependent movements in the IC region of the transporter.

We note that a similar isomerization event was detected in the two 4 μs long simulations initiated from the hDAT^{3TT1} model (Figure 1). Importantly, we found that the inward opening in these simulations followed dynamic trends largely similar to those observed in hDAT^{dDAT} (see Run1 and Run2 in Figure S9).

Inward-Opening Is Related to the PIP$_2$-Mediated N-term/ICL4 Association. As described in Methods, we have developed protocols for quantitative analysis of correlation and clustering of time-dependent variables. Using this analysis, we found, as detailed in a section below, that the isomerization event in the hDAT^{dDAT} trajectory is related to the rise in the PIP$_2$-mediated N-term/ICL4 interactions (see Figure 2A), which, in turn, have a destabilizing effect on the IC network of ionic interactions discussed above (see Figure 3). Similar relationships are observed in the hDAT^{3TT1}Run1 and hDAT^{3TT1}Run2 simulations. For example, in the hDAT^{3TT1}Run2 (Figure S9C), the TM9 segment moves away from TM1a and TM6b within the first 0.5 μs time interval during which the N-term/ICL4 complex is formed (Figure S6A), the IC gates brake open (Figure S6C), and water starts to build up inside the IC vestibule (Figure S9B).

Importantly, an additional 2.2 μs long MD trajectory (Run2ΔPIPb in Figure 1), initiated from the 2.0 μs time-point of hDAT^{3TT1}Run2 (inward-facing conformation) after replacing PIP$_2$ with POPE lipids, showed movement of the ICL4/TM9 segment in the opposite direction, i.e., toward the TM bundle, as the TM1a-TM9 and TM6b-TM9 separations decreased (Figure S9C). Remarkably, we find that the inward movement of TM9 in this simulation was accompanied by dehydration of the IC vestibule (Figure S9B).

Furthermore, in the two control MD trajectories of hDAT carried out in the PIP$_2$-depleted membranes (dDATΔPIP and Run2ΔPIPa), in which the N-term did not engage with the ICL4 (see above) and the IC gates remained closed (Figure S7A−B), there occurred neither significant repositioning of the ICL4/TM9 region with respect to the TM bundle nor an overall opening of the IC vestibule (Figure S7C−D). Collectively, the conformational rearrangements and their spatial and temporal relationships suggest that by destabilizing the IC network of salt bridges, the PIP$_2$-mediated N-term/ICL4 interactions allow a repositioning of the ICL4 and neighboring IC regions so as to trigger an opening of the IC vestibule.

Inward Opening Is Accompanied by Concomitant Movements in the EC Vestibule. Conformational changes occurring on the EC side of the hDAT during the inward opening were evaluated from changes in distances between various EC segments.[39] The time-traces in Figures 5D−E and S10 show that the most prominent motions on the EC side during inward-opening involve the TM1b and TM6a segments that move closer to TM3 (Figure 5D−F). In addition, separation between the ECL4 and ECL6 segments increases (Figure S10E), and the change is related to the repositioning of the ECL4b motif with respect to the TM1b segment whereby F391 (in ECL4b) pulls toward W84 (in TM1b), whereas P387 (in ELC4b) pulls away from W84 (see Figure S11). Notably, these changes are consonant with experimental results reported for the structurally related Na$^+$/proline symporter PutP,[75] which suggested that a pulling motion of the residue in PutP analogous to F391 is a trigger for inward opening. Furthermore, residue W84 in hDAT is analogous to residue W33 in MhsT, the LeuT-fold Na+/hydantoin transporter, where it has been suggested to be mechanistically important for enhancing the transitioning to the inward-facing conformation.[76]

Overall in the hDAT^{dDAT} trajectory, the collective movements result in contraction of the EC vestibule during the transition, as quantified by the decrease in the number of water molecules it accommodates (blue trace in Figure 4B). The specific conformational rearrangements observed in the simulations are consistent with the results from DEER spectroscopy in LeuT[39] showing that the transition to the ligand-bound state involved movements of TM1b and TM6a segments toward TM3 and a repositioning of ECL4 to favor a closed conformation of the EC vestibule. Together, the data presented in Figures 5, S8, and S10 establish that the inward opening in the hDAT^{dDAT} trajectory proceeds through concerted motions on the IC and EC sides of the transporter and involves structural motifs that have been identified experimentally to underlie state-to-state transitions in LeuT.

Isomerization to the Inward-Facing State in hDAT Results in the Release of Na$^+$ Ion from the Na2 Site and Destabilization of the Substrate DA in the S1 Site. Experimental studies have suggested that an inward-closed state is stabilized by a Na$^+$ ion bound in the Na2 site (Na2 ion) in both LeuT[44] and DAT.[55] Computational explorations of dynamics of LeuT,[44,52] DAT,[33] and SERT[56] showed that the isomerization to the inward-facing state induces a destabilization of the ion in the Na2 site. Consistent with these findings, we observe that the transition to the inward-facing state in our simulations is accompanied by the spontaneous release of the Na$^+$ ion from the Na2 site.

The detailed dynamics of Na2 ion in the hDAT^{dDAT} trajectory represented in Figure 6 show that during the first 0.6 μs time interval, the ion in Na2 gradually loses contact with coordinating residues in this site: L418 in TM8 and V78 in TM1 (Figure 6A). This destabilizes the ion in the site, and Na$^+$ leaves the Na2 site via the intracellular vestibule. The path followed by the Na$^+$ ion released from the Na2 site is depicted in Figure 6C−D, highlighting several key residues along the pathway that coordinate the Na$^+$ ion at different time-points of the simulation. Among them, we note D421, T269, and D436, all of which were shown to have functional importance for DAT.[12,36,77]

The destabilization of Na2 was observed as well in the MD simulations initiated from the hDAT^{3TT1} model. As shown in Figure S12, the release of the Na2 ion in Run2 follows largely the same pattern as that in the hDAT^{dDAT} trajectory. Interestingly, in Run1 (Figure S13), the Na$^+$ ion left the Na2 site but remained within the IC vestibule of the transporter for >2 μs trajectory time, ∼5 Å from the Na2 site (and 12 Å away from the Na1 ion, Figure S13B), stabilized by interactions with the side chain of D421 and the catechol moiety of the substrate DA (Figure

DOI: 10.1021/acschemneuro.5b00179
ACS Chem. Neurosci. 2015, 6, 1825−1837

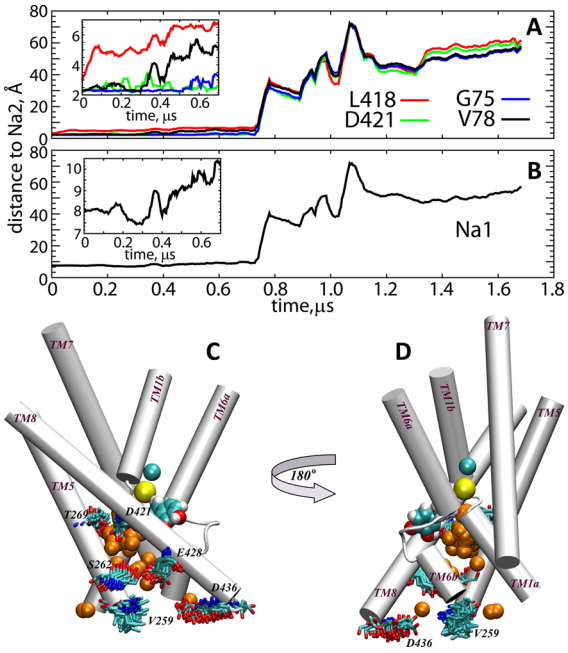

Figure 6. Spontaneous release of the Na^+ ion from the Na2 site during $hDAT^{dDAT}$ simulation. (A) Time-evolution, during the $hDAT^{dDAT}$ run, of minimum distances between the Na^+ ion originally in the Na2 site and its coordinating residues L418 (red), D421 (green), G75 (blue), and V78 (black). (B) The distance between the two Na^+ ions initially in the Na1 and Na2 sites. The insets on panels A and B detail the dynamics of the respective time-dependent variables within the first 0.7 μs time-interval. (C–D) The trajectory of the Na^+ ion (initially in the Na2 site) is traced by the position of the orange spheres. The Na^+ ion in the Na1 site is shown in yellow and the Cl^- ion in cyan. The positions of the ions, the DA ligand (in van der Waals representation), and relevant TM segments of hDAT (in white cartoon rendering) are taken from the initial conformation of the system. The rearrangement of the various residues coordinating the Na2 ion rendered in licorice is identified by their position at different stages of the simulation. The snapshots in panels C and D are related to each other by 180° rotation around the vertical axis (direction perpendicular to the membrane plane).

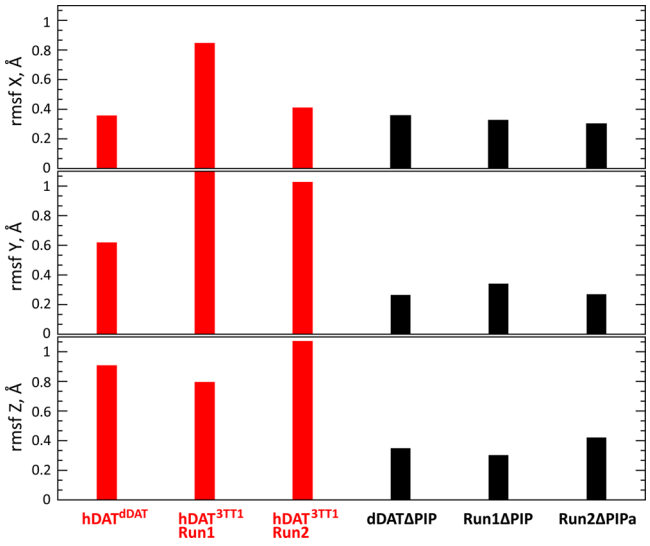

Figure 7. Root-mean square fluctuations (RMSFs) of the substrate DA in the S1 site in the different simulations. For each trajectory, the protein structure at each frame was aligned first to the initial model using the backbone atoms of the TM bundle; the RMSF of the center-of-mass of the DA ring structure was calculated in the three Cartesian coordinates (shown in the three separate panels; see also Figure S14). The data in red and black are from simulations in PIP_2-enriched and in PIP_2-depleted membranes, respectively.

S13D). This finding is consonant with experimental and computational studies that revealed the key role of residue D421 in coordinating the Na^+ ion in the Na2 site.[12]

To evaluate the effect of Na^+ release from the Na2 site on the dynamics of the substrate, DA, in the S1 site, we quantified the root-mean-square fluctuations (RMSFs) in the positional coordinates of the substrate. As shown in Figure 7, we found that the fluctuations in DA positioning are more pronounced in the simulations with PIP_2-containing membranes than in PIP_2-depleted systems in which the inward-opening and Na2 release events were not observed. In particular, in the two simulations ($hDAT^{dDAT}$ and $hDAT^{3TT1}$Run2) in which Na^+ left the transporter, destabilization of the DA substrate leads to its rearrangement in the S1 site so that its ring points toward the IC vestibule (along the z axis, see Figures 7 and S14) and away from TM8 (along the y axis, Figures 7 and S14). In $hDAT^{3TT1}$Run1, the rotation of the substrate ring toward the IC side leads to weakening of interactions between DOP and the S1 site residues (Figure S14C) and allows DOP to engage with the Na^+ ion released from the Na2 site, as described above (see also Figure S13). Gradual destabilization of the substrate as Na^+ diffuses out of the Na2 is consistent with the free energy calculations conducted in LeuT, which suggested that the release of a sodium ion from the Na2 site lowers the energy barrier for substrate uptake.[44]

Correlation Analysis Shows That PIP_2-Mediated N-term/ICL4 Interactions Are Allosterically Coupled to the Functional Sites in hDAT Involved in Inward-Opening Dynamics. We established the relationship between the PIP_2-mediated association of the N-term with ICL4 and the sequence of rearrangements leading to the inward-opening transition associated with (i) the release of the Na^+ ion from the Na2 site and (ii) the destabilization of the substrate DA in the S1 site. To this end, we clustered the time-dependent variable describing PIP_2-mediated N-term/ICL4 contacts (Figure 2A) with the dynamic quantities discussed in Figures 3–6, S8, and S10–S11, using mutual information clustering (MIC). To determine the temporal relationship between the structural motifs that underlie the isomerization event in the hDAT and the PIP_2-controlled N-term/ICL4 dynamics, we identified the dominant clusters (Figure 8) using the FMI measure (see Methods and Figure S15).

The resulting "cluster tree" (dendrogram) shown in Figure 8 is constructed from the dynamic variables described in Figures 3–6, S8, and S10–S11. It shows a large cluster of highly correlated variables (rendered in red) consisting of distance changes on the IC and EC sides of the transporter. The cluster identifies strong temporal correlations between the dynamics of the TM1a/TM6b/ICL4/TM9 segments on the IC end, and the distance changes related to the movements of TM1b/TM6a regions on the EC vestibule combined with the movement of the ECL4b region with respect to TM1b (involving residues W84, F387, and F391). Connected to this limb of the dendrogram is another large branch (shown in blue in Figure 8), which consists mostly of additional dynamic variables that describe the opening of the IC vestibule during isomerization. This branch also contains the PIP_2-mediated N-term/ICL4 contacts ("NT/ICL4 cont." in Figure 8), as well as the dynamics of the Na2 ion.

DOI: 10.1021/acschemneuro.5b00179
ACS Chem. Neurosci. 2015, 6, 1825–1837

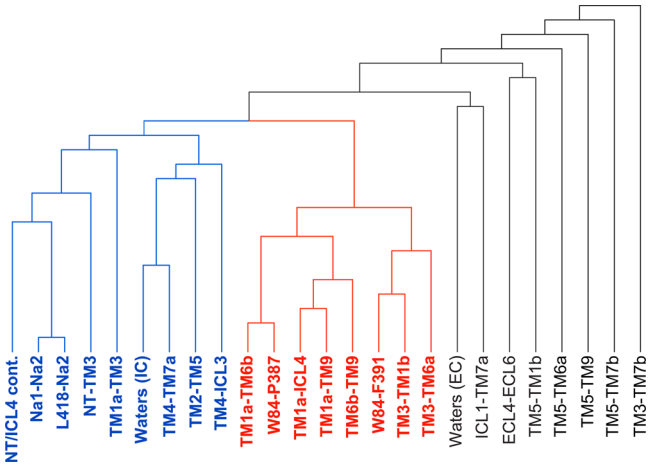

Figure 8. Cluster tree (dendrogram) constructed from the dynamic variables discussed in Figures 3–6, and S8 and S10–S11. The dendrogram shows a merger of two clusters (variables and limbs shown in red and blue) and a connection of the resulting large cluster to smaller branches of the tree (in black). The variables in black are weakly correlated with those belonging to the colored clusters; as assessed by the Fowlkes–Mallows Index, the variables in black do not affect the clustering significantly, (see Methods and also Figure S15).

Clustering analysis on the same quantities extracted from hDAT^{3TT1}Run1 and hDAT^{3TT1}Run2 trajectories (Figure S16) again revealed a merger of two clusters (in red and blue colors) containing various IC and EC structural motifs that describe (i) inward-opening of the transporter (most prominently, dynamics in TM1a/TM6b/ICL4/TM9 segments), (ii) movement of the Na2 ion, (iii) the extent of PIP_2-mediated N-term/ICL4 contacts, and (iv) the dynamics of the ECL4b. We find that in all cases of inward-opening, there is one dominant cluster composed of interhelical distances between TM1a, TM6b, and TM9 (colored in red), which is strongly coupled to a cluster containing the N-term/ICL4 contacts (colored in blue). In this manner, the clustering analysis establishes quantitatively the coupling between the PIP_2-mediated N-term/ICL4 association and the structural hallmarks related to the inward-opening transition in the hDAT.

The prominent role played by the ICL4 region in the inward opening transition prompted a deeper analysis of the manner in which dynamics in the ICL4 propagates to the functional sites of the transporter. To this end, we quantified in the simulated trajectories the extent to which collective motions within the ICL4 segment were allosterically coupled to the collective motions composed of (i) the residues that line the ion binding sites Na1 and Na2 and (ii) the residues in the primary S1 and the presumed secondary S2 substrate binding sites in hDAT. We used a measure of information transmission between multivariate systems with correlated collective fluctuations known as the total intercorrelation, which was developed as part of the N-body Information Theory (NbIT) framework we have described previously (see refs 78 and 79 for details).

The time evolution of the intercorrelation coefficient (r_{INTER}), which quantifies the extent of coupling between the collective motions of the ICL4 region and various functional sites, was calculated from the hDAT^{dDAT}, hDAT^{3TT1}Run1, and hDAT^{3TT1}Run2 trajectories and is shown in Figure 9. Similar plots obtained from the analysis of the simulations in PIP_2-depleted membranes (dDATΔPIP and Run2ΔPIPa) are shown in Figure S17. For completeness, the Supporting Information

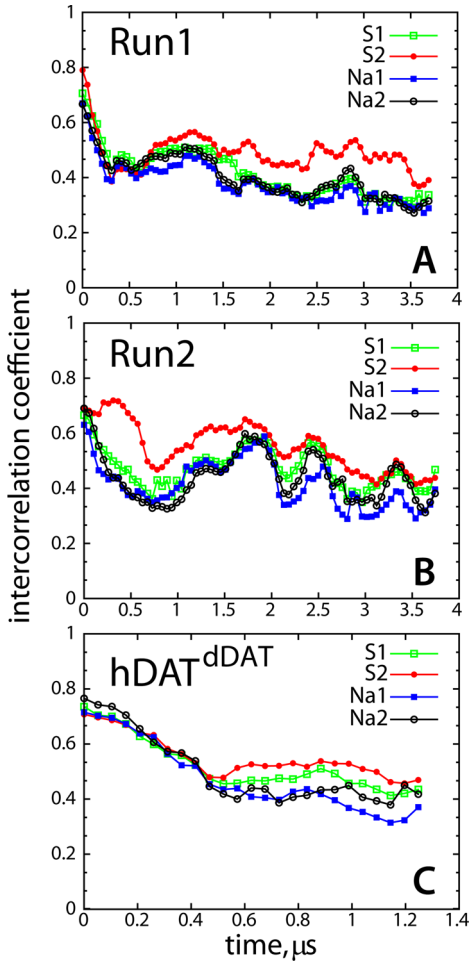

Figure 9. Total intercorrelation coefficient (see eq 5) between the residues in ICL4 and in different functional sites of the hDAT: substrate binding S1 and S2 sites (green and red, respectively); Na^+ ion binding sites Na1 and Na2 (blue and black, respectively). The intercorrelation coefficients are shown separately for simulations Run1 (A), Run2 (B), and hDAT^{dDAT} (C) and were obtained as averages over 500 ns time intervals by sliding the analysis windows by 50 ns (see Methods for more details).

Movie illustrates the time sequence of the corresponding intercorrelation matrix, obtained for the hDAT^{dDAT} system, quantifying the intercorrelation coefficients between all of the pairs of residues considered in the NbIT calculations.

Figure 9 shows the strong coupling (large r_{INTER} values) between the dynamics within the ICL4 segment and the dynamics in the functional sites of the transporter. The values are highest in the initial stages of the hDAT^{dDAT}, hDAT^{3TT1}Run1, and hDAT^{3TT1}Run2 simulations, as the initial 0.5 μs interval coincides in time with the inward-opening in these simulations (see above), but they decrease after the completion of the isomerization event. The results suggest that the isomerization event is associated with highly coupled motions in the ICL4 and the functional regions. In fact, the same analysis performed on dDATΔPIP and Run2ΔPIPa trajectories, for which the initial protein models were the same as in hDAT^{dDAT} and hDAT^{3TT1}Run2 simulations, respectively, but in which the hDAT did not transition to the inward-facing state, revealed relatively small r_{INTER} values (Figure S17), comparable to those after isomerization in the hDAT^{dDAT}, hDAT^{3TT1}Run1, and hDAT^{3TT1}Run2 simulations. This leads to the inference that the

DOI: 10.1021/acschemneuro.5b00179
ACS Chem. Neurosci. 2015, 6, 1825–1837

high correlations measured in the trajectories collected in PIP_2-enriched membranes are indeed related to the transition to the inward-facing state observed in these systems.

Especially notable is the higher value of r_{INTER} for the S2 site (red traces in Figure 9). The S2 site in hDAT includes residues W84, P387, and F391, which as described above (Figure S11) are involved in the conformational rearrangements accompanying the inward opening. In these rearrangements, the specific motion in ECL4b results in a pulling of F391 toward W84, while P387 moves away from W84. Thus, we find that the observed strong correlations between the ICL4 and the S2 site is primarily due to highly coupled motions in the ICL4 segment and the S2 residues from the ECL4b loop, adjacent to P387, that participate in the described pulling motion analogous to that observed in PutP.[75] This is illustrated in the Supporting Information Movie and identified by the clustering analysis.

Figure 9 also shows that after the initial decrease in the correlations, the coupling between the ICL4 and some of the functional sites exhibits positive fluctuations in the $hDAT^{dDAT}$, $hDAT^{3TT1}$Run1, and $hDAT^{3TT1}$Run2 systems. The timing of the increase in correlations shown in Figure 9 coincides with the event of Na^+ release from the Na2 site (at ~0.75, 1.25, and 1.0 μs time-points in the 3 simulations $hDAT^{dDAT}$, $hDAT^{3TT1}$Run1, and $hDAT^{3TT1}$Run2 systems, respectively). After the release is complete, we observe a slow relaxation of the correlations (see $hDAT^{3TT1}$Run2 in Figure 9), with the coupling between ICL4 and the S2 site remaining the highest among all the correlations considered. Collectively, the NbIT analysis demonstrates and quantifies the allosteric coupling between the ICL4 and the functional sites during the PIP_2-mediated inward-opening of the hDAT, and identifies the S2 site as the region with the strongest coupling to the ICL4, suggesting that this distant communication is mechanistically important for the inward-opening transition.

N-Terminus as an Important Allosteric Modulator of the Functional Inward-Opening in hDAT. The results presented above addresses, to our knowledge for the first time, the mechanistic involvement of the N-terminal region of the hDAT in the functionally relevant conformational transitions of the transporter involved in the inward-opening of the hDAT. Thus, novel molecular-level mechanistic insights about the PIP_2 lipid-mediated dynamics of the hDAT N-terminus in functionally relevant state-to-state transitions in the transporter suggest specific steps of the spontaneous transition of the hDAT from the initially outward-facing conformation to the inward-facing state. Interestingly, the rearrangements observed in specific structural motifs parallel those identified previously in LeuT and are found to culminate in the release of Na^+ ion from the functional Na2 site and the destabilization of the substrate in the S1 site.

The results show that the conformational isomerization triggered by the strong tendency of the N-term to associate with the ICL4 segment through PIP_2-mediated electrostatic interactions involves the H442/R443/H443 triad of polar residues in the ICL4 and the set of basic residues in the N-term. The mechanistic consequences of the PIP_2-mediated N-term/ICL4 association that emerge from this analysis are the disruption of a conserved IC network of ionic interactions, which triggers the inward-opening by destabilizing the IC network of ionic interactions, and the associated release of the Na^+ ion from the Na2 site causes destabilization of the substrate DA in the primary S1 site.

Taken together, the simulation results suggest how the N-term/ICL4 association driven by the interaction with PIP_2 facilitates the isomerization of hDAT to the inward-facing state. The structural hallmarks of this isomerization in our simulations are similar to those identified experimentally to underlie functionally relevant transitions in the LeuT-like NSS proteins. Moreover, results implicating interactions between the N-term and ICL4 segments in the inward-opening isomerization of the hDAT construct are consonant with experimental studies in the GABA transporter (GAT1) in which the same two regions have been shown to modulate forward as well as reverse substrate transport.[80,81]

The atomistic details of the computational modeling show that the mechanism for the N-term interaction with the PIP_2-containing membrane involves charged residues both at the distal (i.e., the very N-terminal part) end of the segment (residues K3 and K5 in particular) and the proximal end (near TM1 of the transmembrane bundle) of the segment (and especially R51). It is known that specific charge-neutralization mutations in the N-term, either K3A/K5A or R51W, do not affect regular substrate transport but do interfere with amphetamine-dependent efflux.[11,71] The simulations identify the contacts between PIP_2 and R51 as leading to the association of R51 with the ICL4 residues and show that the interactions between PIP_2 and K3/K5 lead to an anchoring of the distal part of the N-term to the membrane surface (as in the $hDAT^{dDAT}$ and $hDAT^{3TT1}$Run2 simulations), which has been suggested to enable the N-term phosphorylation required for AMPH-induced efflux.[71] In the $hDAT^{3TT1}$Run1 trajectory, this drives N-term/ICL4 complex formation.

These detailed observations from the multiple simulations can explain why the experimentally measured substrate uptake is not necessarily impaired when efflux is reduced by mutation. In the $hDAT^{3TT1}$Run1 trajectory, it appears that the charged K3/K5 distal segment can also drive N-term/ICL4 complex formation in the absence of phosphorylation so that the PIP_2-mediated N-term/ICL4 association may be sustained in the hDAT construct bearing either the K3A/K5A or the R51W mutation separately and that both the K3A/K5A hDAT and the R51W hDAT constructs could transition toward the inward-facing state through this mechanism.

The consequences of these interactions for the functional mechanism of the transporter are underscored by our findings showing that inward opening is accompanied by concomitant movements in the EC vestibule and that isomerization to the inward-facing state in hDAT results in the release of the Na^+ ion from the Na2 site and the destabilization of the substrate (DA) in the S1 site. Indeed, our analysis using the tools offered by the NbIT framework[78,79] identified the allosteric connection showing that collective motions triggered by the N-term/ICL4 association on the intracellular side are strongly coupled to collective motions in the extracellular vestibule and in the substrate and ion binding sites. Further substantiating the mechanistic importance of the PIP_2-mediated N-term/ICL4 interactions, their effect on the intracellular side emerged clearly from the MIC results showing that they are allosterically coupled to the functional sites in hDAT involved in inward-opening dynamics. Thus, the MIC revealed a strongly coupled helical bundle (composed of TM1a, TM6b, and TM9) in the intracellular side that was highly correlated to the N-term/ICL4 association, suggesting how the N-term can modulate the stability of this bundle and thus modulate intracellular gating. In combination, these results identify the N-terminus as an important allosteric modulator of the functional inward-opening and ion/substrate release in hDAT.

DOI: 10.1021/acschemneuro.5b00179
ACS Chem. Neurosci. 2015, 6, 1825−1837

Direct effects of the N-term interaction with PIP_2 in the function of hDAT had been inferred from the various experimental studies cited throughout. Some of these studies have demonstrated that the PIP_2-sequestering basic peptide (palpeptide) competes with the hDAT N-term to bind PIP_2-enriched liposomes[71] and that cell perfusion with palpeptide impairs AMPH-induced DA efflux but not the regular DA uptake.[71] However, the interpretation of such results is rendered somewhat difficult by the possible involvement of other proteins and various plasma membrane components that are known to regulate functional mechanisms in hDAT; specifically, palpeptide treatment is very likely to affect as well the spatial organization of such membrane components. Indeed, colocalization of hDAT with effector proteins such as Flot1 and STX within plasma membrane microdomains is known to be important for AMPH-induced substrate efflux but not for the uptake.[70] In turn, STX in neuronal cells is found to reside inside PIP_2-enriched plasma membrane compartments,[82] suggesting that the effects of PIP_2-sequestering palpeptide may stem, at least in part, from disruption of these functional domains. These considerations bring to light the importance of future attempts to broaden the scope of structure−function studies to include rigorous molecular-level mechanistic investigations of DAT and the NSS molecular machines within the rich environments that are relevant to their function.

METHODS

Molecular Modeling of hDAT. *Homology Model of the hDAT Transmembrane Bundle.* Several molecular models of the full-length hDAT (residues 1−620) were prepared for all-atom MD simulations in explicit lipid membranes and water environments. Briefly, we used Modeler 9v10[83] and a previously published sequence alignment of the NSS-family proteins[31] to first construct homology models for the TM part of the hDAT (contained in residues 57−590) based on either the outward-facing dDAT structure (PDB code: 4M48),[20] or on the high resolution outward-open X-ray structure of the bacterial member of the NSS family, LeuT (PDB code: 3TT1).[22] As described in detail,[12,55] the models included the substrate, dopamine (DA), docked in the S1 site, two Na^+ ions, positioned equivalently to those in the LeuT crystal structure, and a Cl^- ion coordinated by residues Asn82, Tyr102, Ser321, and Asn353 of hDAT, based on the chloride binding site described previously.[32,84]

PROPKA 3.0[85] was used to determine the protonation states of ionizable residues of hDAT and resulted in Glu491 being protonated. Furthermore, a disulfide bond was introduced in EL2, between Cys180 and Cys189, according to available structural and functional information. More details about the models can be found in refs 12 and 55.

Ab Initio Modeling of hDAT Termini. Structural information regarding the terminal domains of the DAT or of other NSS proteins is lacking. Indeed, the X-ray models of the dDAT does not include the N-term, whereas the C-term is only partially resolved. Therefore, we generated and tested 3D models of the structurally unknown N- and C-terminal domains of the hDAT (fragments 1−57 and 591−620, respectively, that lack sequence homology to proteins of known fold) as described earlier,[72] using Rosetta-based *ab initio* structure prediction algorithms. Briefly, different fragments of the termini were subjected to the Rosetta *ab initio* fold prediction routine, and for each construct, the predicted structures were clustered under various residue exclusion conditions. Clusters containing the majority of structures were identified. The conformations in the top clusters were evaluated with the RMSDTT iterative fitting algorithm[86] to find regions with the highest structural conservation within each cluster, and the folds with the lowest scores (from the Rosetta energy function) in each cluster were selected.

As described in our recent work,[72] the protocol described above identified two structured elements in this fragment (Figure S1), an α-helical region and a β-sheet motif, that were stable in long time-scale (~2.2 μs) MD simulations. When the same set of computational tools was applied to the folding of the C-terminus of hDAT, α-helices were predicted in this region as well (Figure S2), consistent with the X-ray structure of the dDAT in which a large part of the C-terminus that is present is helical. More details of the *ab initio* modeling of the terminal domains are presented in ref 72.

The predicted structures for the N- and C-termini were docked (using Modeler 9v10[83]) onto the two models of the hDAT TM bundle described above to complete the full-length hDAT models based on dDAT and LeuT (referred to throughout as $hDAT^{dDAT}$ and $hDAT^{3TT1}$, respectively; see Figure S3). Since the X-ray model of the dDAT does not inform on the mutual orientations of the two termini, we considered for the $hDAT^{3TT1}$ model two alternative docking poses, resulting in two starting conformations for subsequent MD simulations, in which the relative positioning of the N- and C-termini were different (see Figure S3A). For the $hDAT^{dDAT}$ model, only one docking pose was considered in which the positioning of the C-terminus closely followed that in the dDAT X-ray structure, and the N-terminus was docked so as not to contact any residue in the TM bundle (Figure S3B).

hDAT-Membrane Complexes. $hDAT^{dDAT}$ and $hDAT^{3TT1}$ models were immersed into a pre-equilibrated membrane[72] containing an asymmetric lipid distribution of 451 lipids between the two leaflets so as to resemble a lipid composition of neuronal cell plasma membranes:[87] 100:40:32:27:29 mixture of POPE/POPC/PIP_2/POPS/cholesterol on the intracellular leaflet and 176:29:18 mixture of POPC/DPPC/cholesterol on the extracellular leaflet.

For each transporter-embedded membrane patch, lipids overlapping with the protein were removed so that the overall lipid fractions were retained. After solvating with TIP3P water, the transporter−membrane complexes were neutralized with either K^+Cl^- or Na^+Cl^- as specified in Results and Discussion (see Figure 1 captions), resulting in a final atom count of ~150,000.

Molecular Dynamics Simulations. Simulations of the $hDAT^{dDAT}$ and $hDAT^{3TT1}$ constructs in the corresponding membrane environments were initiated with the previously established multistep equilibration protocol[44] carried out with NAMD software, version 2.9.[88] During this stage, the backbone of the protein was first fixed and then harmonically constrained. The solvent was initially prevented from entering the lipid−water interface. The constraints on the protein backbone were released gradually in three steps of 300 ps each, changing the force constants from 1, to 0.5, and 0.1 kcal/ (mol $Å^2$), respectively. This step was followed by relatively short (50−100 ns) unbiased MD simulations performed with a 2 fs integration time-step and under the *NPT* ensemble (at T = 310 K), using the Particle-Mesh-Ewald (PME) method for electrostatics[89] and the Nose−Hoover Langevin piston[88] to control the target 1 atm pressure, with Langevin piston period and decay parameters set to 100 and 50 fs, respectively.

After this equilibration phase, long, microsecond-scale unbiased MD simulations were initiated on the Acellera GPU cluster that runs the specialized MD simulation software ACEMD.[90] ACEMD allows computations with standard CHARMM force fields, and for all the runs (including the equilibration phases with the NAMD described above), we used the all-atom CHARMM27 force field for proteins with CMAP corrections,[91] the CHARMM36 force field for lipids,[92] the TIP3P water model, and the CHARMM-compatible force-field parameter set for PIP_2 lipids.[93] For the simulations with ACEMD, we implemented the PME method for electrostatic calculations and carried them out according to the protocol developed at Acellera[90] with a 4 fs integration time-step with a standard mass repartitioning procedure for hydrogen atoms implemented in ACEMD. The computations were conducted under the *NVT* ensemble (at T = 310 K), using the Langevin Thermostat with Langevin Damping Factor set to 0.1. More details about MD simulations with ACEMD can be found in ref 90.

The production times for the two runs with the $hDAT^{3TT1}$ model and the run with the $hDAT^{dDAT}$ construct are listed in Figure 1. As detailed in Figure 1, at different time-points along these trajectories we depleted the PIP_2 lipids by replacing them with POPE lipids. After short (5000 step) minimization, these new systems were subjected to long unbiased MD simulations (see Figure 1 for time-scales). All the trajectories were

DOI: 10.1021/acschemneuro.5b00179
ACS Chem. Neurosci. 2015, 6, 1825−1837

analyzed using a combination of VMD,[94] R software,[95] and various analyses tools developed in-house.

Calculating the Number of Water Molecules in the EC and IC Vestibules of hDAT. Following an algorithm used in our previous work,[46] a water molecule is considered to be in the EC vestibule if (a) its oxygen atom is within 26 Å of the C_β atom of F326 but not within 5 Å of lipid atoms and (b) if its z-coordinate is larger than the C_β atom of F326 by no more than 23 Å (the *z*-axis is perpendicular to the membrane with its positive direction toward the EC side). Similarly, the algorithm assumes that a water molecule belongs to the IC vestibule if its oxygen atom is within 15 Å of the ligand dopamine but not within 5 Å of any lipid and if its z-coordinate is larger than that of the C_β atom of D436 by no more than 15.5 Å.

Correlation and Clustering Analysis of Time-Dependent Variables. The temporal correlation between time-dependent variables extracted from the MD simulations was quantified by calculating the Pearson correlation coefficients between the pairs of variables. To cluster the dynamic quantities based on the strength of temporal correlations between them, we then performed agglomerative mutual-hierarchical clustering[96] on the matrix of correlation coefficients, using mutual information as the distance criterion, as described in ref 96. The linear approximation of the mutual information was calculated and corrected for dimensionality using the generalized correlation coefficient.[97] Briefly, the clustering algorithm first assigns each variable to its own branch and then calculates the pairwise generalized correlation coefficient between all branches. Two branches with the highest correlation are then merged, and the generalized correlation coefficient between the new branch and all other branches are recalculated. The algorithm continues until all variables are members of the same branch. In our application here, the dendrogram (tree) is built from the small number of medium-sized clusters consisting of highly correlated variables. The moderately correlated clusters are then merged into one large cluster. Finally, the tree is completed with the remaining small clusters that are weakly correlated to both each other and the large cluster.

In order to distinguish quantitatively between mergers of different sized clusters, we used the FMI[98] as a measure of similarity between the different clustering before and after each merger. The FMI is defined as

$$B = \frac{\sum_i \sum_j m_{ij}^2 - n}{\sqrt{(\sum_i (\sum_j m_{ij})^2 - n)(\sum_j (\sum_i m_{ij})^2 - n)}} \quad (1)$$

In the above equation, n is the number of objects being clustered, and m is a matrix with rows equal to the number of clusters in the premerger clustering, columns equal to the number of clusters in the postmerger clustering, and elements m_{ij} equaling the number of common members in cluster i of the premerger clustering and cluster j of the postmerger clustering. The FMI ranges from 0 to 1, with low values indicating the merger of similarly sized clusters that significantly change the clustering and high values describing mergers that do not change the overall clustering, such as the joining of small clusters (compared to other existing clusters) to each other or to a larger cluster. Therefore, the mergers of the medium-sized clusters will have relatively low FMI, whereas the mergers of small clusters to the large cluster (as is observed at the end of the clustering) will have a high FMI.

Using NbIT to Calculate the Time-Dependent Total Intercorrelation Coefficient. In order to calculate the time-dependent total intercorrelation coefficient, we used the computational framework in the recently developed NbIT (N-body Information Theory) analysis methodology.[78,79] Briefly, subsets of the full trajectories are generated using sliding windows, beginning a new 500 ns subset every 50 ns. For each subset, the total intercorrelation between specific regions of the protein is calculated as described in ref 79. First, for each set of residues of interest, the set is considered as a 3N-dimensional multivariate distribution, where N is the number of non-hydrogen atoms in the set, and the multivariate normal approximation of the differential entropy H is calculated from the non-hydrogen atomic fluctuation covariance matrix using Carma[99] and in-house software. Next, the total intercorrelation between set A and B is calculated as

$$TC_{\mathrm{INTER}}(A, B) = TC(A, B) - TC(A|B) - TC(B|A) \quad (2)$$

where $TC(A,B)$ is the total correlation of the joint distribution of A and B, and $TC(A|B)$ and $TC(B|A)$ is the total correlation of A conditional on B and the total correlation of B conditional on A, respectively. The total correlation is defined as

$$TC(A) = \sum_{i=1}^{d_A} H(A_i) - H(A) \quad (3)$$

where d_A is the dimension of distribution A, and A_i is the i-th dimension of A. The conditional total correlation is defined as

$$\mathrm{TC}(A|B) = \sum_{i=1}^{d_A} (H(A_i, B) - H(B)) - (H(A, B) - H(B)) \quad (4)$$

The total intercorrelation is then expressed as the total intercorrelation coefficient, r_{INTER}, which ranges from from 0 to 1

$$r_{\mathrm{INTER}}(A, B) = \sqrt{1 - e^{-2TC_{\mathrm{INTER}}(A,B)/d_A + d_B - 1}} \quad (5)$$

■ ASSOCIATED CONTENT

Supporting Information

The Supporting Information is available free of charge on the ACS Publications website at DOI: 10.1021/acschemneuro.5b00179.

Seventeen supporting figures (PDF)

Intercorrelation coefficient simulation of hDAT^{dDAT} (AVI)

■ AUTHOR INFORMATION

Corresponding Author

*Department of Physiology and Biophysics, WCMC, 1300 York Avenue, Room LC-501B, New York, NY 10065. Phone: 212-746-6539. Fax: 212-746-6226. E-mail: gek2009@med.cornell.edu.

Funding

This work was supported by the National Institutes of Health grants P01DA012408, R01DA035263, and U54GM087519. J.M. is supported by the "Caja Madrid" Graduate Fellowship and the "La Caixa" Graduate Fellowship. M.V.L. is supported by a Ruth L. Kirschstein National Research Service Award F31DA035533.

Notes

The authors declare no competing financial interest.

■ ACKNOWLEDGMENTS

Illuminating discussions with Professors Aurelio Galli, Jonathan Javitch, and Ulrik Gether are gratefully acknowledged. The following computational resources are gratefully acknowledged: the Acellera supercomputer cluster at Barcelona Biomedical Research Park; an XSEDE allocation at the Texas Advanced Computing Center at the University of Texas at Austin (Stampede supercomputer, projects TG-MCB090132, and TG-MCB120008); resources of the Oak Ridge Leadership Computing Facility (ALCC allocation BIP109) at the Oak Ridge National Laboratory, which is supported by the Office of Science of the U.S. Department of Energy under Contract No. DE-AC05-00OR22725; and an allocation at the National Energy Research Scientific Computing Center (NERSC, repository m1710, used for initial studies) supported by the Office of Science of the U.S. Department of Energy under Contract No. DE-AC02-05CH11231. The computational resources of the David A. Cofrin Center for Biomedical Information in the HRH

DOI: 10.1021/acschemneuro.5b00179
ACS Chem. Neurosci. 2015, 6, 1825−1837

Prince Alwaleed Bin Talal Bin Abdulaziz Alsaud Institute for Computational Biomedicine were used for the information theory-based analysis of collective motions and correlations.

REFERENCES

(1) Kanner, B. I., and Zomot, E. (2008) Sodium-coupled neurotransmitter transporters. *Chem. Rev. 108*, 1654−1668.
(2) Focke, P. J., Wang, X., and Larsson, H. P. (2013) Neurotransmitter transporters: structure meets function. *Structure 21*, 694−705.
(3) Broer, S., and Gether, U. (2012) The solute carrier 6 family of transporters. *Br. J. Pharmacol. 167*, 256−278.
(4) Rudnick, G., Kramer, R., Blakely, R. D., Murphy, D. L., and Verrey, F. (2014) The SLC6 transporters: perspectives on structure, functions, regulation, and models for transporter dysfunction. *Pfluegers Arch. 466*, 25−42.
(5) Kristensen, A. S., Andersen, J., Jorgensen, T. N., Sorensen, L., Eriksen, J., Loland, C. J., Stromgaard, K., and Gether, U. (2011) SLC6 neurotransmitter transporters: structure, function, and regulation. *Pharmacol Rev. 63*, 585−640.
(6) Pramod, A. B., Foster, J., Carvelli, L., and Henry, L. K. (2013) SLC6 transporters: structure, function, regulation, disease association and therapeutics. *Mol. Aspects Med. 34*, 197−219.
(7) Chen, N. H., Reith, M. E., and Quick, M. W. (2004) Synaptic uptake and beyond: the sodium- and chloride-dependent neurotransmitter transporter family SLC6. *Pfluegers Arch. 447*, 519−531.
(8) Sora, I., Li, B., Fumushima, S., Fukui, A., Arime, Y., Kasahara, Y., Tomita, H., and Ikeda, K. (2009) Monoamine transporter as a target molecule for psychostimulants. *Int. Rev. Neurobiol 85*, 29−33.
(9) Sulzer, D., Sonders, M. S., Poulsen, N. W., and Galli, A. (2005) Mechanisms of neurotransmitter release by amphetamines: a review. *Prog. Neurobiol. 75*, 406−433.
(10) Robertson, S. D., Matthies, H. J., and Galli, A. (2009) A closer look at amphetamine-induced reverse transport and trafficking of the dopamine and norepinephrine transporters. *Mol. Neurobiol. 39*, 73−80.
(11) Cartier, E., Hamilton, P., Belovich, A. N., Shekar, A., Campbell, N. G., Saunders, C., Andreassen, T. F., Gether, U., Veenstra-Vanderweele, J., Sutcliffe, J. S., Ulery-Reynolds, P. G., Erreger, K., Matthies, H. J., and Galli, A. (2015) Rare Autism-Associated Variants Implicate Syntaxin 1 (STX1 R26Q) Phosphorylation and the Dopamine Transporter (hDAT R51W) in Dopamine Neurotransmission and Behaviors. *EBioMedicine 2*, 135−146.
(12) Hansen, F. H., Skjorringe, T., Yasmeen, S., Arends, N. V., Sahai, M. A., Erreger, K., Andreassen, T. F., Holy, M., Hamilton, P. J., Neergheen, V., Karlsborg, M., Newman, A. H., Pope, S., Heales, S. J., Friberg, L., Law, I., Pinborg, L. H., Sitte, H. H., Loland, C., Shi, L., Weinstein, H., Galli, A., Hjermind, L. E., Möller, L. B., and Gether, U. (2014) Missense dopamine transporter mutations associate with adult parkinsonism and ADHD. *J. Clin. Invest. 124*, 3107−3120.
(13) Hamilton, P. J., Campbell, N. G., Sharma, S., Erreger, K., Herborg Hansen, F., Saunders, C., Belovich, A. N., Sahai, M. A., Cook, E. H., Gether, U., McHaourab, H. S., Matthies, H. J., Sutcliffe, J. S., and Galli, A. (2013) De novo mutation in the dopamine transporter gene associates dopamine dysfunction with autism spectrum disorder. *Mol. Psychiatry 18*, 1315−1323.
(14) Sakrikar, D., Mazei-Robison, M. S., Mergy, M. A., Richtand, N. W., Han, Q., Hamilton, P. J., Bowton, E., Galli, A., Veenstra-Vanderweele, J., Gill, M., and Blakely, R. D. (2012) Attention deficit/hyperactivity disorder-derived coding variation in the dopamine transporter disrupts microdomain targeting and trafficking regulation. *J. Neurosci. 32*, 5385−5397.
(15) Bowton, E., Saunders, C., Erreger, K., Sakrikar, D., Matthies, H. J., Sen, N., Jessen, T., Colbran, R. J., Caron, M. G., Javitch, J. A., Blakely, R. D., and Galli, A. (2010) Dysregulation of dopamine transporters via dopamine D2 autoreceptors triggers anomalous dopamine efflux associated with attention-deficit hyperactivity disorder. *J. Neurosci. 30*, 6048−6057.
(16) Mazei-Robison, M. S., Bowton, E., Holy, M., Schmudermaier, M., Freissmuth, M., Sitte, H. H., Galli, A., and Blakely, R. D. (2008) Anomalous dopamine release associated with a human dopamine transporter coding variant. *J. Neurosci. 28*, 7040−7046.
(17) Ng, J., Zhen, J., Meyer, E., Erreger, K., Li, Y., Kakar, N., Ahmad, J., Thiele, H., Kubisch, C., Rider, N. L., Morton, D. H., Strauss, K. A., Puffenberger, E. G., D'Agnano, D., Anikster, Y., Carducci, C., Hyland, K., Rotstein, M., Leuzzi, V., Borck, G., Reith, M. E., and Kurian, M. A. (2014) Dopamine transporter deficiency syndrome: phenotypic spectrum from infancy to adulthood. *Brain 137*, 1107−1119.
(18) Bowton, E., Saunders, C., Reddy, I. A., Campbell, N. G., Hamilton, P. J., Henry, L. K., Coon, H., Sakrikar, D., Veenstra-VanderWeele, J. M., Blakely, R. D., Sutcliffe, J., Matthies, H. J., Erreger, K., and Galli, A. (2014) SLC6A3 coding variant Ala559Val found in two autism probands alters dopamine transporter function and trafficking. *Transl. Psychiatry 4*, e464.
(19) Mergy, M. A., Gowrishankar, R., Gresch, P. J., Gantz, S. C., Williams, J., Davis, G. L., Wheeler, C. A., Stanwood, G. D., Hahn, M. K., and Blakely, R. D. (2014) The rare DAT coding variant Val559 perturbs DA neuron function, changes behavior, and alters in vivo responses to psychostimulants. *Proc. Natl. Acad. Sci. U. S. A. 111*, E4779−4788.
(20) Penmatsa, A., Wang, K. H., and Gouaux, E. (2013) X-ray structure of dopamine transporter elucidates antidepressant mechanism. *Nature 503*, 85−90.
(21) Penmatsa, A., Wang, K. H., and Gouaux, E. (2015) X-ray structures of Drosophila dopamine transporter in complex with nisoxetine and reboxetine. *Nat. Struct. Mol. Biol. 22*, 506−508.
(22) Krishnamurthy, H., and Gouaux, E. (2012) X-ray structures of LeuT in substrate-free outward-open and apo inward-open states. *Nature 481*, 469−474.
(23) Wang, H., Elferich, J., and Gouaux, E. (2012) Structures of LeuT in bicelles define conformation and substrate binding in a membrane-like context. *Nat. Struct. Mol. Biol. 19*, 212−219.
(24) Piscitelli, C. L., and Gouaux, E. (2012) Insights into transport mechanism from LeuT engineered to transport tryptophan. *EMBO J. 31*, 228−235.
(25) Wang, H., and Gouaux, E. (2012) Substrate binds in the S1 site of the F253A mutant of LeuT, a neurotransmitter sodium symporter homologue. *EMBO Rep. 13*, 861−866.
(26) Piscitelli, C. L., Krishnamurthy, H., and Gouaux, E. (2010) Neurotransmitter/sodium symporter orthologue LeuT has a single high-affinity substrate site. *Nature 468*, 1129−1132.
(27) Singh, S. K., Piscitelli, C. L., Yamashita, A., and Gouaux, E. (2008) A competitive inhibitor traps LeuT in an open-to-out conformation. *Science 322*, 1655−1661.
(28) Singh, S. K., Yamashita, A., and Gouaux, E. (2007) Antidepressant binding site in a bacterial homologue of neurotransmitter transporters. *Nature 448*, 952−956.
(29) Yamashita, A., Singh, S. K., Kawate, T., Jin, Y., and Gouaux, E. (2005) Crystal structure of a bacterial homologue of Na+/Cl− dependent neurotransmitter transporters. *Nature 437*, 215−223.
(30) Penmatsa, A., and Gouaux, E. (2014) How LeuT shapes our understanding of the mechanisms of sodium-coupled neurotransmitter transporters. *J. Physiol. 592*, 863−869.
(31) Beuming, T., Shi, L., Javitch, J. A., and Weinstein, H. (2006) A comprehensive structure-based alignment of prokaryotic and eukaryotic neurotransmitter/Na+ symporters (NSS) aids in the use of the LeuT structure to probe NSS structure and function. *Mol. Pharmacol. 70*, 1630−1642.
(32) Kantcheva, A. K., Quick, M., Shi, L., Winther, A. M., Stolzenberg, S., Weinstein, H., Javitch, J. A., and Nissen, P. (2013) Chloride binding site of neurotransmitter sodium symporters. *Proc. Natl. Acad. Sci. U. S. A. 110*, 8489−8494.
(33) Shan, J., Javitch, J. A., Shi, L., and Weinstein, H. (2011) The substrate-driven transition to an inward-facing conformation in the functional mechanism of the dopamine transporter. *PLoS One 6*, e16350.
(34) Guptaroy, B., Zhang, M., Bowton, E., Binda, F., Shi, L., Weinstein, H., Galli, A., Javitch, J. A., Neubig, R. R., and Gnegy, M. E. (2009) A juxtamembrane mutation in the N terminus of the dopamine transporter

DOI: 10.1021/acschemneuro.5b00179
ACS Chem. Neurosci. 2015, 6, 1825−1837

induces preference for an inward-facing conformation. *Mol. Pharmacol. 75*, 514−524.
(35) Beuming, T., Kniazeff, J., Bergmann, M. L., Shi, L., Gracia, L., Raniszewska, K., Newman, A. H., Javitch, J. A., Weinstein, H., Gether, U., and Loland, C. J. (2008) The binding sites for cocaine and dopamine in the dopamine transporter overlap. *Nat. Neurosci. 11*, 780−789.
(36) Kniazeff, J., Shi, L., Loland, C. J., Javitch, J. A., Weinstein, H., and Gether, U. (2008) An intracellular interaction network regulates conformational transitions in the dopamine transporter. *J. Biol. Chem. 283*, 17691−17701.
(37) Stockner, T., Montgomery, T. R., Kudlacek, O., Weissensteiner, R., Ecker, G. F., Freissmuth, M., and Sitte, H. H. (2013) Mutational analysis of the high-affinity zinc binding site validates a refined human dopamine transporter homology model. *PLoS Comput. Biol. 9*, e1002909.
(38) Jardetzky, O. (1966) Simple allosteric model for membrane pumps. *Nature 211*, 969−970.
(39) Kazmier, K., Sharma, S., Quick, M., Islam, S. M., Roux, B., Weinstein, H., Javitch, J. A., and McHaourab, H. S. (2014) Conformational dynamics of ligand-dependent alternating access in LeuT. *Nat. Struct. Mol. Biol. 21*, 472−479.
(40) Zhao, Y., Terry, D., Shi, L., Weinstein, H., Blanchard, S. C., and Javitch, J. A. (2010) Single-molecule dynamics of gating in a neurotransmitter transporter homologue. *Nature 465*, 188−193.
(41) Zhao, Y., Terry, D. S., Shi, L., Quick, M., Weinstein, H., Blanchard, S. C., and Javitch, J. A. (2011) Substrate-modulated gating dynamics in a Na+-coupled neurotransmitter transporter homologue. *Nature 474*, 109−113.
(42) Claxton, D. P., Quick, M., Shi, L., de Carvalho, F. D., Weinstein, H., Javitch, J. A., and McHaourab, H. S. (2010) Ion/substrate-dependent conformational dynamics of a bacterial homolog of neurotransmitter:sodium symporters. *Nat. Struct. Mol. Biol. 17*, 822−829.
(43) Kazmier, K., Sharma, S., Islam, S. M., Roux, B., and McHaourab, H. S. (2014) Conformational cycle and ion-coupling mechanism of the Na+/hydantoin transporter Mhp1. *Proc. Natl. Acad. Sci. U. S. A. 111*, 14752−14757.
(44) Shi, L., Quick, M., Zhao, Y., Weinstein, H., and Javitch, J. A. (2008) The mechanism of a neurotransmitter:sodium symporter−inward release of Na+ and substrate is triggered by substrate in a second binding site. *Mol. Cell 30*, 667−677.
(45) Quick, M., Shi, L., Zehnpfennig, B., Weinstein, H., and Javitch, J. A. (2012) Experimental conditions can obscure the second high-affinity site in LeuT. *Nat. Struct. Mol. Biol. 19*, 207−211.
(46) Zhao, C., Stolzenberg, S., Gracia, L., Weinstein, H., Noskov, S., and Shi, L. (2012) Ion-controlled conformational dynamics in the outward-open transition from an occluded state of LeuT. *Biophys. J. 103*, 878−888.
(47) Quick, M., Winther, A. M., Shi, L., Nissen, P., Weinstein, H., and Javitch, J. A. (2009) Binding of an octylglucoside detergent molecule in the second substrate (S2) site of LeuT establishes an inhibitor-bound conformation. *Proc. Natl. Acad. Sci. U. S. A. 106*, 5563−5568.
(48) Zomot, E., Gur, M., and Bahar, I. (2015) Microseconds Simulations Reveal a New Sodium-Binding Site and the Mechanism of Sodium-Coupled Substrate Uptake by LeuT. *J. Biol. Chem. 290*, 544.
(49) Cheng, M. H., and Bahar, I. (2014) Complete mapping of substrate translocation highlights the role of LeuT N-terminal segment in regulating transport cycle. *PLoS Comput. Biol. 10*, e1003879.
(50) Cheng, M. H., and Bahar, I. (2013) Coupled global and local changes direct substrate translocation by neurotransmitter-sodium symporter ortholog LeuT. *Biophys. J. 105*, 630−639.
(51) Li, J., Shaikh, S. A., Enkavi, G., Wen, P. C., Huang, Z., and Tajkhorshid, E. (2013) Transient formation of water-conducting states in membrane transporters. *Proc. Natl. Acad. Sci. U. S. A. 110*, 7696−7701.
(52) Shaikh, S. A., and Tajkhorshid, E. (2010) Modeling and dynamics of the inward-facing state of a Na+/Cl- dependent neurotransmitter transporter homologue. *PLoS Comput. Biol. 6*, e1000905.
(53) Li, J., and Tajkhorshid, E. (2009) Ion-releasing state of a secondary membrane transporter. *Biophys. J. 97*, L29−31.
(54) Celik, L., Schiott, B., and Tajkhorshid, E. (2008) Substrate binding and formation of an occluded state in the leucine transporter. *Biophys. J. 94*, 1600−1612.
(55) Borre, L., Andreassen, T. F., Shi, L., Weinstein, H., and Gether, U. (2014) The second sodium site in the dopamine transporter controls cation permeation and is regulated by chloride. *J. Biol. Chem. 289*, 25764−25773.
(56) Koldso, H., Autzen, H. E., Grouleff, J., and Schiott, B. (2013) Ligand induced conformational changes of the human serotonin transporter revealed by molecular dynamics simulations. *PLoS One 8*, e63635.
(57) Khoshbouei, H., Sen, N., Guptaroy, B., Johnson, L., Lund, D., Gnegy, M. E., Galli, A., and Javitch, J. A. (2004) N-terminal phosphorylation of the dopamine transporter is required for amphetamine-induced efflux. *PLoS Biol. 2*, E78.
(58) Fog, J. U., Khoshbouei, H., Holy, M., Owens, W. A., Vaegter, C. B., Sen, N., Nikandrova, Y., Bowton, E., McMahon, D. G., Colbran, R. J., Daws, L. C., Sitte, H. H., Javitch, J. A., Galli, A., and Gether, U. (2006) Calmodulin kinase II interacts with the dopamine transporter C terminus to regulate amphetamine-induced reverse transport. *Neuron 51*, 417−429.
(59) Giambalvo, C. T. (1992) Protein kinase C and dopamine transport−2. Effects of amphetamine in vitro. *Neuropharmacology 31*, 1211−1222.
(60) Giambalvo, C. T. (2003) Differential effects of amphetamine transport vs. dopamine reverse transport on particulate PKC activity in striatal synaptoneurosomes. *Synapse 49*, 125−133.
(61) Foster, J. D., Pananusorn, B., Cervinski, M. A., Holden, H. E., and Vaughan, R. A. (2003) Dopamine transporters are dephosphorylated in striatal homogenates and in vitro by protein phosphatase 1. *Mol. Brain Res. 110*, 100−108.
(62) Foster, J. D., Pananusorn, B., and Vaughan, R. A. (2002) Dopamine transporters are phosphorylated on N-terminal serines in rat striatum. *J. Biol. Chem. 277*, 25178−25186.
(63) Kahlig, K. M., Javitch, J. A., and Galli, A. (2004) Amphetamine regulation of dopamine transport. Combined measurements of transporter currents and transporter imaging support the endocytosis of an active carrier. *J. Biol. Chem. 279*, 8966−8975.
(64) Kahlig, K. M., Binda, F., Khoshbouei, H., Blakely, R. D., McMahon, D. G., Javitch, J. A., and Galli, A. (2005) Amphetamine induces dopamine efflux through a dopamine transporter channel. *Proc. Natl. Acad. Sci. U. S. A. 102*, 3495−3500.
(65) Dipace, C., Sung, U., Binda, F., Blakely, R. D., and Galli, A. (2007) Amphetamine induces a calcium/calmodulin-dependent protein kinase II-dependent reduction in norepinephrine transporter surface expression linked to changes in syntaxin 1A/transporter complexes. *Mol. Pharmacol. 71*, 230−239.
(66) Binda, F., Dipace, C., Bowton, E., Robertson, S. D., Lute, B. J., Fog, J. U., Zhang, M., Sen, N., Colbran, R. J., Gnegy, M. E., Gether, U., Javitch, J. A., Erreger, K., and Galli, A. (2008) Syntaxin 1A interaction with the dopamine transporter promotes amphetamine-induced dopamine efflux. *Mol. Pharmacol. 74*, 1101−1108.
(67) Foster, J. D., Cervinski, M. A., Gorentla, B. K., and Vaughan, R. A. (2006) Regulation of the dopamine transporter by phosphorylation. *Handb Exp Pharmacol*, 197−214.
(68) Thwar, P. K., Guptaroy, B., Zhang, M., Gnegy, M. E., Burns, M. A., and Linderman, J. J. (2007) Simple transporter trafficking model for amphetamine-induced dopamine efflux. *Synapse 61*, 500−514.
(69) Torres, B., and Ruoho, A. E. (2014) N-terminus regulation of VMAT2 mediates methamphetamine-stimulated efflux. *Neuroscience 259*, 194−202.
(70) Cremona, M. L., Matthies, H. J., Pau, K., Bowton, E., Speed, N., Lute, B. J., Anderson, M., Sen, N., Robertson, S. D., Vaughan, R. A., Rothman, J. E., Galli, A., Javitch, J. A., and Yamamoto, A. (2011) Flotillin-1 is essential for PKC-triggered endocytosis and membrane microdomain localization of DAT. *Nat. Neurosci. 14*, 469−477.
(71) Hamilton, P. J., Belovich, A. N., Khelashvili, G., Saunders, C., Erreger, K., Javitch, J. A., Sitte, H. H., Weinstein, H., Matthies, H. J., and

DOI: 10.1021/acschemneuro.5b00179
ACS Chem. Neurosci. 2015, 6, 1825−1837

Galli, A. (2014) PIP2 regulates psychostimulant behaviors through its interaction with a membrane protein. *Nat. Chem. Biol. 10*, 582−589.
(72) Khelashvili, G., Doktorova, M., Sahai, M. A., Johner, N., Shi, L., and Weinstein, H. (2015) Computational modeling of the N-terminus of the human dopamine transporter and its interaction with PIP2 -containing membranes. *Proteins: Struct., Funct., Genet. 83*, 952−969.
(73) Buchmayer, F., Schicker, K., Steinkellner, T., Geier, P., Stubiger, G., Hamilton, P. J., Jurik, A., Stockner, T., Yang, J. W., Montgomery, T., Holy, M., Hofmaier, T., Kudlacek, O., Matthies, H. J., Ecker, G. F., Bochkov, V., Galli, A., Boehm, S., and Sitte, H. H. (2013) Amphetamine actions at the serotonin transporter rely on the availability of phosphatidylinositol-4,5-bisphosphate. *Proc. Natl. Acad. Sci. U. S. A. 110*, 11642−11647.
(74) Stolzenberg, S., Quick, M., Zhao, C., Gotfryd, K., Khelashvili, G., Gether, U., Loland, C. J., Javitch, J. A., Noskov, S., Weinstein, H., and Shi, L. (2015) Mechanism of the Association between Na+ Binding and Conformations at the Intracellular Gate in Neurotransmitter:Sodium Symporters. *J. Biol. Chem. 290*, 13992.
(75) Raba, M., Dunkel, S., Hilger, D., Lipiszko, K., Polyhach, Y., Jeschke, G., Bracher, S., Klare, J. P., Quick, M., Jung, H., and Steinhoff, H. J. (2014) Extracellular loop 4 of the proline transporter PutP controls the periplasmic entrance to ligand binding sites. *Structure 22*, 769−780.
(76) Malinauskaite, L., Quick, M., Reinhard, L., Lyons, J. A., Yano, H., Javitch, J. A., and Nissen, P. (2014) A mechanism for intracellular release of Na(+) by neurotransmitter/sodium symporters. *Nat. Struct. Mol. Biol. 21*, 1006−1012.
(77) Itokawa, M., Lin, Z., Cai, N. S., Wu, C., Kitayama, S., Wang, J. B., and Uhl, G. R. (2000) Dopamine transporter transmembrane domain polar mutants: DeltaG and DeltaDeltaG values implicate regions important for transporter functions. *Mol. Pharmacol. 57*, 1093−1103.
(78) LeVine, M. V., and Weinstein, H. (2014) NbIT–a new information theory-based analysis of allosteric mechanisms reveals residues that underlie function in the leucine transporter LeuT. *PLoS Comput. Biol. 10*, e1003603.
(79) LeVine, M. V., Perez-Aguilar, J. M., and Weinstein, H. (2014) N-body Information Theory (NbIT) Analysis of Rigidi-Body Dynamics in Intracellular Loop 2 of the 5-HT2A Receptor. *Proc. IWBBIO, Granada*, 7−9.
(80) Deken, S. L., Beckman, M. L., Boos, L., and Quick, M. W. (2000) Transport rates of GABA transporters: regulation by the N-terminal domain and syntaxin 1A. *Nat. Neurosci 3*, 998−1003.
(81) Hansra, N., Arya, S., and Quick, M. W. (2004) Intracellular domains of a rat brain GABA transporter that govern transport. *J. Neurosci. 24*, 4082−4087.
(82) van den Bogaart, G., Meyenberg, K., Risselada, H. J., Amin, H., Willig, K. I., Hubrich, B. E., Dier, M., Hell, S. W., Grubmuller, H., Diederichsen, U., and Jahn, R. (2011) Membrane protein sequestering by ionic protein-lipid interactions. *Nature 479*, 552−555.
(83) Eswar, N., Webb, B., Marti-Renom, M. A., Madhusudhan, M. S., Eramian, D., Shen, M. Y., Pieper, U., Sali, A. (2006) Comparative protein structure modeling using Modeller, *Curr. Protoc Bioinformatics Chapter 5*, Unit 5.6.10.1002/0471250953.bi0506s15
(84) Zomot, E., Bendahan, A., Quick, M., Zhao, Y., Javitch, J. A., and Kanner, B. I. (2007) Mechanism of chloride interaction with neurotransmitter:sodium symporters. *Nature 449*, 726−730.
(85) Olsson, M. H. M., Sondergaard, C. R., Rostkowski, M., and Jensen, J. H. (2011) PROPKA3: Consistent Treatment of Internal and Surface Residues in Empirical pKa Predictions. *J. Chem. Theory Comput. 7*, 525−537.
(86) Gracia, L. (2005) *RMSDTT: RMSD Trajectory Tool*, 2.5 ed., Weill Medical College of Cornell University, Department of Physiology and Biophysics, New York.
(87) Ariga, T., Macala, L. J., Saito, M., Margolis, R. K., Greene, L. A., Margolis, R. U., and Yu, R. K. (1988) Lipid composition of PC12 pheochromocytoma cells: characterization of globoside as a major neutral glycolipid. *Biochemistry 27*, 52−58.
(88) Phillips, J. C., Braun, R., Wang, W., Gumbart, J., Tajkhorshid, E., Villa, E., Chipot, C., Skeel, R. D., Kale, L., and Schulten, K. (2005) Scalable molecular dynamics with NAMD. *J. Comput. Chem. 26*, 1781−1802.
(89) Essmann, U., Perera, L., Berkowitz, M. L., Darden, T., Lee, H., and Pedersen, L. G. (1995) A Smooth Particle Mesh Ewald Method. *J. Chem. Phys. 103*, 8577−8593.
(90) Harvey, M., Giupponi, G., and De Fabritiis, G. (2009) ACEMD: Accelerated molecular dynamics simulations in the microseconds timescale. *J. Chem. Theory Comput. 5*, 1632−1639.
(91) Brooks, B. R., Brooks, C. L., 3rd, Mackerell, A. D., Jr., Nilsson, L., Petrella, R. J., Roux, B., Won, Y., Archontis, G., Bartels, C., Boresch, S., Caflisch, A., Caves, L., Cui, Q., Dinner, A. R., Feig, M., Fischer, S., Gao, J., Hodoscek, M., Im, W., Kuczera, K., Lazaridis, T., Ma, J., Ovchinnikov, V., Paci, E., Pastor, R. W., Post, C. B., Pu, J. Z., Schaefer, M., Tidor, B., Venable, R. M., Woodcock, H. L., Wu, X., Yang, W., York, D. M., and Karplus, M. (2009) CHARMM: the biomolecular simulation program. *J. Comput. Chem. 30*, 1545−1614.
(92) Klauda, J. B., Venable, R. M., Freites, J. A., O'Connor, J. W., Tobias, D. J., Mondragon-Ramirez, C., Vorobyov, I., MacKerell, A. D., and Pastor, R. W. (2010) Update of the CHARMM All-Atom Additive Force Field for Lipids: Validation on Six Lipid Types. *J. Phys. Chem. B 114*, 7830−7843.
(93) Lupyan, D., Mezei, M., Logothetis, D. E., and Osman, R. (2010) A molecular dynamics investigation of lipid bilayer perturbation by PIP2. *Biophys. J. 98*, 240−247.
(94) Humphrey, W., Dalke, A., and Schulten, K. (1996) VMD: visual molecular dynamics. *J. Mol. Graphics 14*, 33−38 27−38.
(95) R Core Team (2013) *R: A Language and Environment for Statistical Computing*, R Foundation for Statistical Computing, Vienna, Austria, http://www.R-project.org/.
(96) Kraskov, A., Stögbauer, H., Andrzejak, R. G., and Grassberger, P. (2005) Hierarchical clustering using mutual information. *Europhys. Lett. 70*, 278−284.
(97) Lange, O. F., and Grubmuller, H. (2006) Generalized correlation for biomolecular dynamics. *Proteins: Struct., Funct., Genet. 62*, 1053−1061.
(98) Fowlkes, E. B., and Mallows, C. L. (1983) A Method for Comparing Two Hierarchical Clusterings. *J. Am. Stat. Assoc. 78*, 553−569.
(99) Glykos, N. M. (2006) Software news and updates. Carma: a molecular dynamics analysis program. *J. Comput. Chem. 27*, 1765−1768.

DOI: 10.1021/acschemneuro.5b00179
ACS Chem. Neurosci. 2015, 6, 1825−1837